Kovove Mater. 60 2022 181–189
DOI: 10.31577/km.2022.3.181

Comparison of the microstructure of ERNiCrFe-7A deposited metal by cold wire GTAW and hot wire GTAW

Haiyang Zhu[1,2], Kun Liu[1], Xiangping Xu[1], Jiasheng Zou[1]*

[1] *School of Materials Science and Engineering, Jiangsu University of Science and Technology, Zhenjiang 212003, P. R. China*
[2] *Department of Metallurgical and Materials Engineering, Suzhou Institute of Technology, Jiangsu University of Science and Technology, Soochow 215000, P. R. China*

Received 19 December 2021, received in revised form 31 March 2022, accepted 18 May 2022

Abstract

ERNiCrFe-7A filler metal is widely used for welding Inconel 690 alloy, which is often considered for fabricating key components such as reactor pressure vessel and steam generator of nuclear island main equipment. In this work, ERNiCrFe-7A deposited metal was prepared by cold wire and hot wire GTAW process separately. The microstructure and mechanism of precipitation of deposited metal were studied by OM, XRD, SEM, and TEM. Results show that both cold wire and hot wire GTAW can get good quality of ERNiCrFe-7A deposited metal. The matrix of deposited metal is γ-austenite. The microstructure of deposited metal has a cellular dendritic characteristic. The intragranular precipitates are MX phases (M = Nb and Ti, X = C and/or N), and the intergranular precipitates are Cr-rich $M_{23}C_6$ phases. The heat input of cold wire GTAW is higher than that of hot wire GTAW, the columnar grains by cold wire GTAW are wider than those of hot wire GTAW, and the number of MX and $M_{23}C_6$ phases by cold wire GTAW is more than that by hot wire GTAW.

K e y w o r d s: ERNiCrFe-7A, deposited metal, microstructure, cold wire GTAW, hot wire GTAW

1. Introduction

Inconel 690 nickel-base alloy has high resistance to primary water stress corrosion cracking (PWSCC), intergranular stress corrosion cracking (ISCC), and good comprehensive performance, which is widely used in the manufacture of key components such as reactor pressure vessel and steam generator of the third generation nuclear island main equipment [1].

ERNiCrFe-7A, also known as filler metal 52M, is commonly used for welding Inconel 690, dissimilar metals, and overlays [2–5]. The Gas Tungsten Arc Welding (GTAW) process is a versatile fusion welding process that can weld most materials, including manual GTAW, automatic GTAW, and hot wire GTAW [6]. Conventional automatic GTAW is also called cold wire GTAW (CW-GTAW). Hot wire GTAW (HW-GTAW) is a modified GTAW process in which the filler metal is preheated by resistance heating using a separate power source. HW-GTAW has the advantages of high deposition rate, low heat input, and small distortion [7, 8].

At present, manual GTAW and CW-GTAW processes have been widely used in welding ERNiCrFe-7A filler metal, and a large number of studies have been carried out on the microstructure and properties [9–13]. Because of higher production efficiency, the HW-GTAW process is gradually replacing CW-GTAW in manufacturing nuclear equipment [14]. However, the differences in microstructure of the two different processes are not fully clear, especially the microstructure characteristic of HW-GTAW. This work studied the microstructure differences of ERNiCrFe-7A deposited metal by HW-GTAW compared with CW-GTAW.

2. Materials and experimental procedure

The filler metal was ERNiCrFe-7A of 1.2 mm in diameter, with the nominal chemical composition given

*Corresponding author: e-mail address: zjzoujs@126.com

T a b l e 1. Nominal chemical composition of the filler metal (wt.%)

Material	C	Si	Mn	Cr	Fe	Mo	Nb+Ta	Al	Ti	Ni
ERNiCrFe-7A	0.04	0.5	1.0	28.0–31.5	7.0–11.0	0.5	0.5–1.0	1.1	1.0	Bal

T a b l e 2. Welding parameters

Sample	U (V)	I (A)	I_W (A)	S (mm min^{-1})	WFR (mm min^{-1})	Heat input (J mm^{-1})
CW-GTAW	12	260	–	110	1500	1702
HW-GTAW	12	240	20	110	2000	1578

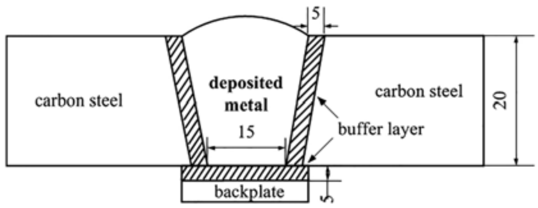

Fig. 1. Schematic of a welded joint.

in Table 1. Deposited metal was fabricated using butt weld by CW-GTAW and HW-GTAW. The dimension of the single plate was 350 × 100 × 20 mm^3. Plates were prepared as single V grooved joint with a 10° bevel angle and supported with a backplate (Fig. 1). The groove surface and backplate were buttered with ERNiCrFe-7A filler metal in order to keep the deposited metal undiluted. The deposited metal by CW-GTAW involved 10 layers and 24 weld passes, while 9 layers and 20 weld passes by HW-GTAW.

The welding parameters are listed in Table 2. Heat input of CW-GTAW and HW-GTAW was calculated separately using the following Eqs. (1) and (2). Heat input of CW-GTAW consisted of arc heat ($U \times I$), while HW-GTAW consisted of arc heat ($U \times I$) and resistance heat ($I^2 \times R$):

$$\text{CW-GTAW: Heat input} = \frac{UI}{S}, \qquad (1)$$

$$\text{HW-GTAW: Heat input} = \frac{UI + I_W^2 R}{S}, \qquad (2)$$

where U (V) is arc voltage, I (A) is arc current, S (mm s^{-1}) is travel speed, I_W(A) is hot wire current, and $R(\Omega)$ is wire resistance. $R = \rho\frac{L}{A}$, ρ (Ω m) is wire resistivity, (ρ = 1.148E–6), L (m sec^{-1}) is wire feed length (L = WFR/60 000), WFR (mm min^{-1}) is Wire Feed Rate, and A(m^2) is the cross-sectional area of the wire.

The heat input of CW-GTAW was 1702 J mm^{-1}, higher than 1578 J mm^{-1} of HW-GTAW.

The cross-sectional samples of deposited metal were obtained by wire electrical discharge machine. After grinding and polishing, the surface was etched using a solution of 10 g $CuSO_4$, 50 ml HCl, and 50 ml H_2O. The microstructure of deposited metal was observed by optical microscope (OM). The matrix phase was analyzed by X-ray diffractometer (XRD). The precipitated phase of deposited metal was analyzed by scanning electron microscopy (SEM), energy dispersive spectroscopy (EDS), and transmission electron microscopy (TEM). The thin foils of TEM samples were polished using an electrolyte of 7 % $HClO_4$, 4 % CH_3COOH, and 89 % C_2H_5OH.

3. Results

3.1. Grain analysis

The macroscopic metallographic morphologies of deposited metal by CW-GTAW and HW-GTAW are shown in Figs. 2a,c. There are no cracks, incomplete penetrations, pores, and other defects. The columnar crystal orientation is obvious, growing in the temperature gradient direction, perpendicular to the welding layer interface. The columnar crystal trend of CW-GTAW is more apparent than that of HW-GTAW, especially in the central region. Because of higher heat input by CW-GTAW, the cooling solidification rate of the molten pool becomes smaller. The undercooling degree decreases, resulting in reduced nucleus growth and nucleation rate. Due to the nucleation rate being lower than the nucleus growth rate, the number of nuclei per area reduces, and grains coarsen [15].

Figures 2b,d show the center zone microstructures of deposited metal by CW-GTAW and HW-GTAW. The microstructures present typical cellular dendritic characteristics. The grains length is about several millimeters, and the width of the grains by CW-GTAW is roughly 50–200 μm, while 20–150 μm by HW-GTAW. There are some subgrains in the deposited metal of HW-GTAW. Three different types of grain boundary (GB) are found: solidification grain boundary

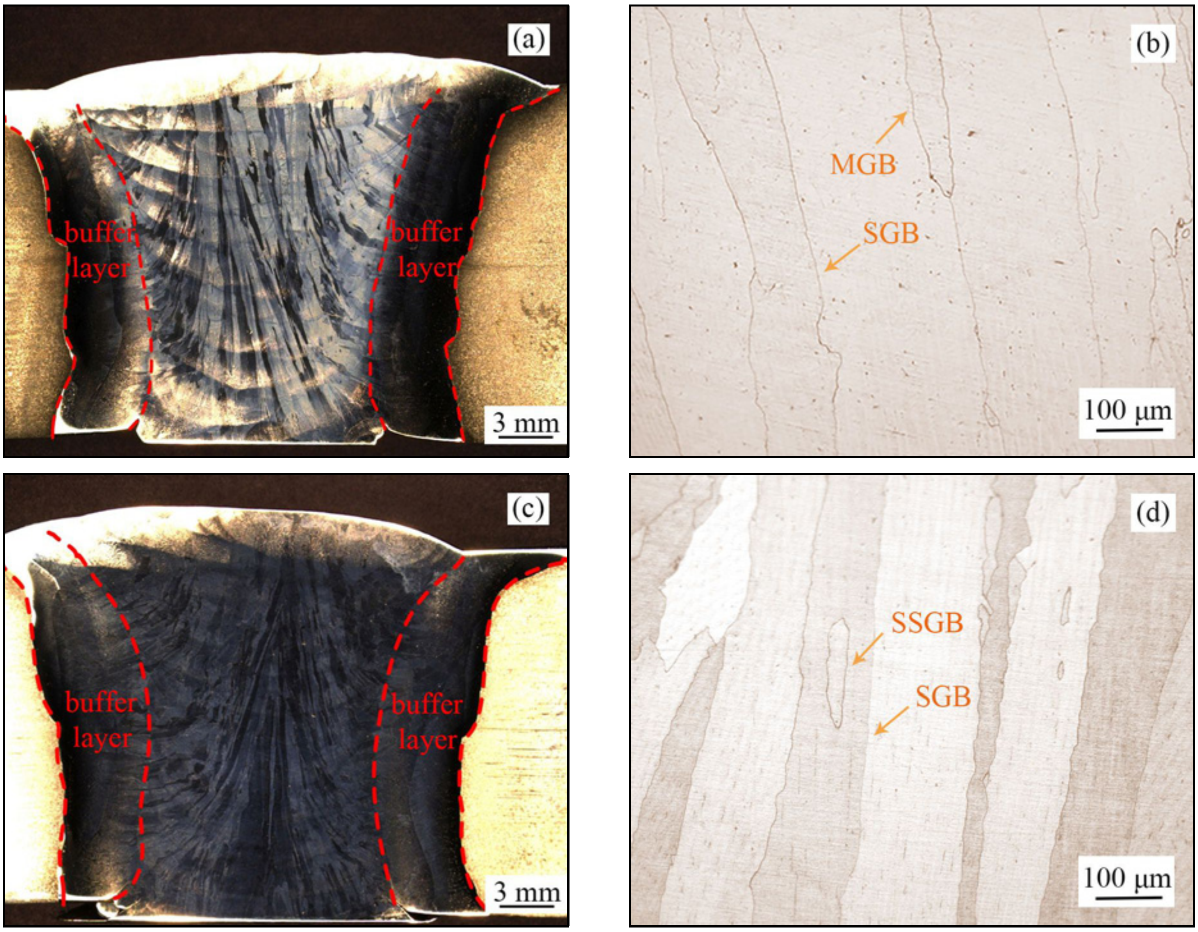

Fig. 2. Macrostructure and microstructure of deposited metal: (a) macrostructure by CW-GTAW, (b) center zone microstructure, (c) macrostructure by HW-GTAW, and (d) center zone microstructure.

(SGB), solidification subgrain boundary (SSGB), and migrated grain boundary (MGB). SSGBs separate these cellular grains or dendrites due to the micro-segregation during the solidification process. MGBs are the grain boundaries that migrate due to solute atoms diffusing across and along the SGBs [16, 17].

3.2. Matrix phase analysis

The XRD patterns of deposited metal by CW-GTAW and HW-GTAW are shown in Fig. 3. The matrix of deposited metal by CW-GTAW is γ-austenite, similar to HW-GTAW. The diffraction peaks of precipitates are not presented; possibly, the X-ray diffraction characteristic peaks of these precipitations are covered by base peak owing to the less content.

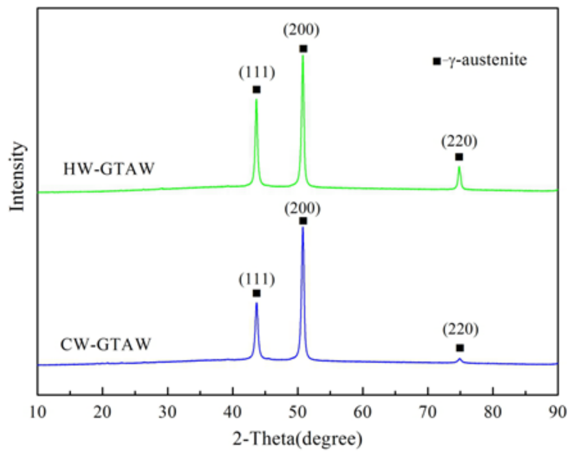

Fig. 3. XRD patterns of deposited metal by CW-GTAW and HW-GTAW.

3.3. Precipitates analysis

Figure 4 is a SEM microstructure image of deposited metal by CW-GTAW and HW-GTAW. Single round or chain particles precipitate in the interdendritic segregation region. The size of large round particles is about 0.5–1 μm. The number of these round precipitates by CW-GTAW is about 30, significantly more than 20 by HW-GTAW. The results of EDS surface scanning analysis show that these large precipitates are rich in Nb and Ti elements (Fig. 5), and the content of Nb is more than that of Ti, while the

Table 3. Results of EDS composition analysis in Fig. 6 (wt.%)

Deposited metal	Points in Fig. 6	Suggested phase	Nb	Ti	C	N	Cr	Ni	Fe	Others
CW-GTAW	1	(Nb,Ti)(C,N)	2.58	5.88	5.64	23.14	20.00	35.31	6.69	Mn 0.76
	2	(Nb,Ti)C	2.30	7.24	6.86	–	26.17	46.14	8.84	Al 2.45
	3	$M_{23}C_6$	0.87	0.21	14.14	–	30.22	45.77	8.44	Si 0.35
	4	$M_{23}C_6$	0.91	–	14.68	–	29.73	45.00	8.59	Si 0.34, Mn 0.75
	5	Matrix	0.95	–	3.99	–	28.83	55.22	9.96	Mn 1.05
HW-GTAW	6	(Nb,Ti)(C,N)	3.13	5.47	8.01	21.22	19.55	33.77	6.04	Al 1.87, Mg 0.94
	7	(Nb,Ti)C	2.05	2.24	5.39	–	30.51	50.34	9.46	–
	8	$M_{23}C_6$	1.20	–	10.47	–	29.67	49.74	8.93	–
	9	Matrix	0.92	–	11.59	–	26.80	50.80	9.12	Mn 0.77

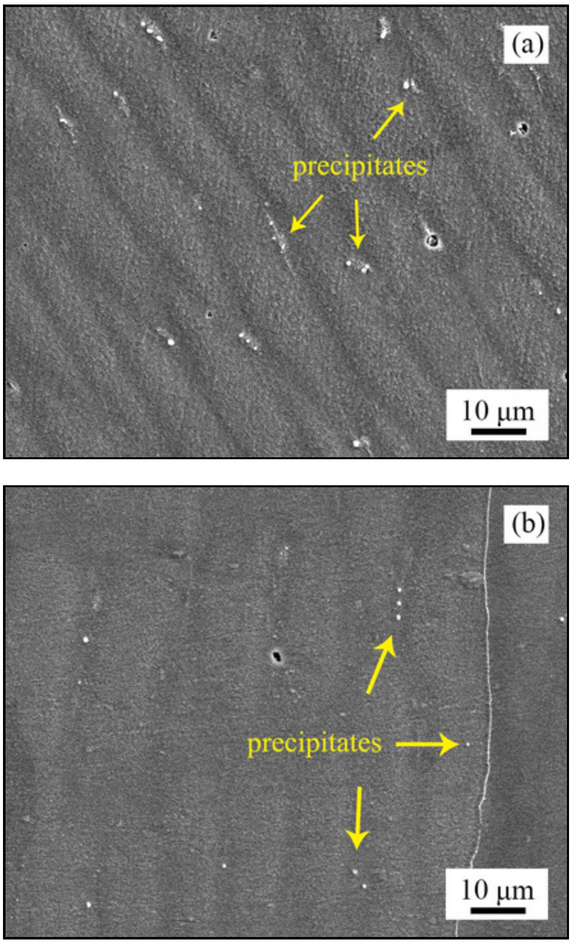

Fig. 4. SEM microstructure image of deposited metal: (a) CW-GTAW, (b) HW-GTAW.

dispersively distributed particles around these large particles are mainly rich in Nb.

The high-fold images of intragranular and intergranular precipitates are shown in Fig. 6. Different sizes of particle phases disperse in grains. Lamellar or blocky phases precipitate along grain boundaries, and some precipitates agglomerate, forming a continuous thin film on grain boundaries. The film width of grain boundary by CW-GTAW is about 230 nm, larger than 190 nm by HW-GTAW (Figs. 6c,d).

Intragranular and intergranular precipitates are analyzed by EDS (Table 3). Intragranular precipitates are speculated to be MX-type carbides (M = Nb and Ti, X = C and/or N), which are (Nb,Ti)(C,N) or (Nb,Ti)C [4, 18–20]. TiN is generally considered nucleation of (Nb,Ti)(C,N). Figure 7 is a TEM bright-field image and selected area electron diffraction (SAED) pattern of TiN in deposited metal. TiN precipitates firstly during solidification, which could not be the core of austenite heterogeneous nucleation due to its large mismatch with the austenite matrix. These precipitates are enriched in the interdendritic region and transformed into Ti(C,N). Ti(C,N) would be transformed into (Nb,Ti)(C,N) at the final stage of solidification, with Nb also segregated in the interdendritic region [21]. Figure 8 is the TEM image of (Nb,Ti)C in deposited metal; the formation of MX carbides may take TiC as a nucleation particle except for TiN. NbC grows up wrapping TiC, the lattice type and lattice constant of TiC and NbC are uniform, and these two phases may dissolve each other and become (Nb,Ti)C [22, 23].

The intergranular precipitates are Cr-rich carbides (Table 3), which are $M_{23}C_6$ by TEM (Fig. 9). $M_{23}C_6$ precipitates maintain a one-sided coherent and one-sided non-coherent relationship with the austenite matrix, causing a high interfacial energy and stress concentration between the semi-coherent interface [1, 24]. Because the heat input of CW-GTAW is higher, the cooling rate of the molten pool is relatively slower, and the precipitation time of $M_{23}C_6$ is relatively longer, resulting in more $M_{23}C_6$ precipitation by CW-GTAW than HW-GTAW.

4. Discussion

The precipitates of ERNiCrFe-7A deposited metal by CW-GTAW and HW-GTAW are two main types:

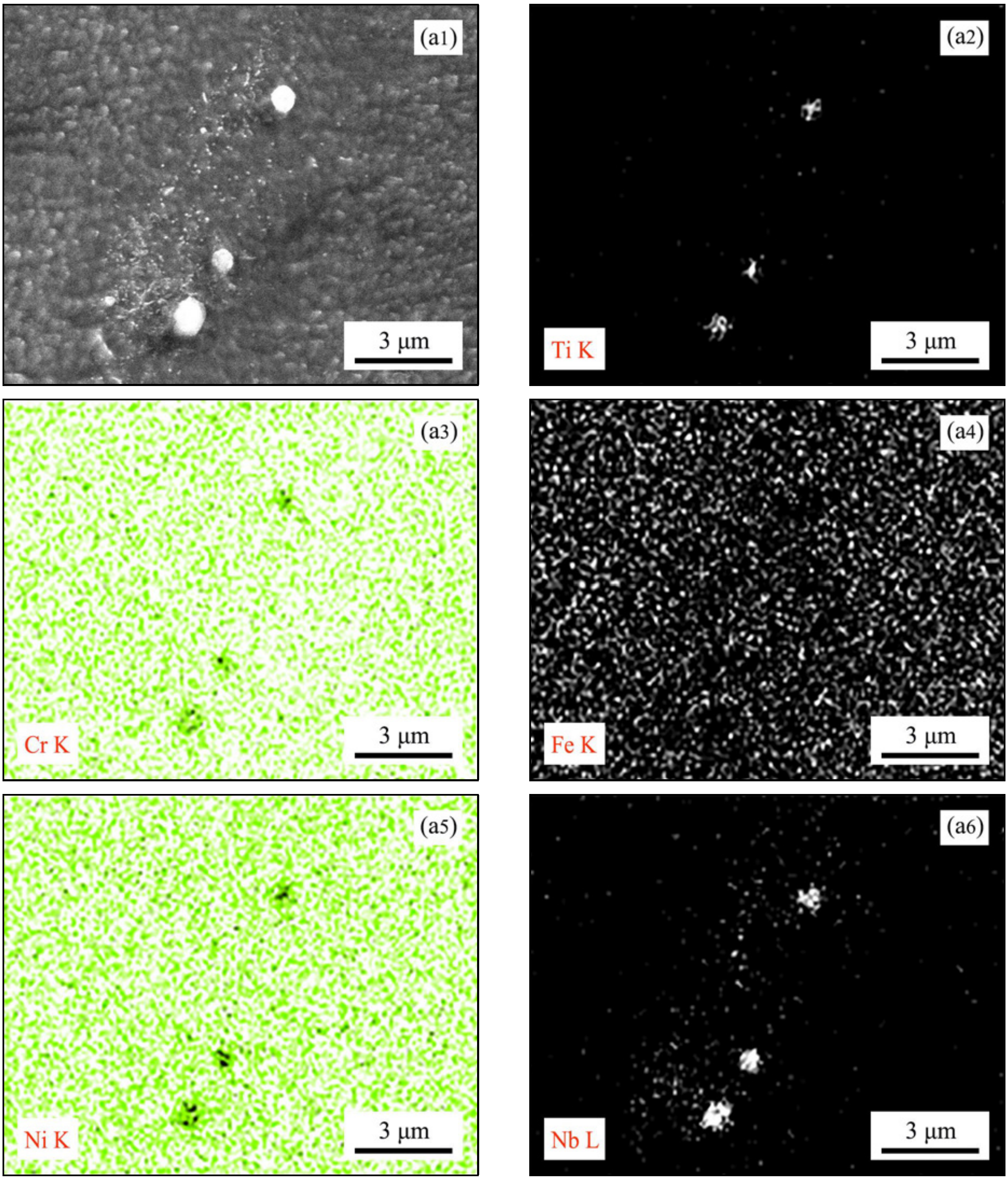

Fig. 5. Map analysis of precipitates by EDS: (a1) SEM image of precipitates, (a2–a6) results of element distribution.

one is Nb-rich and Ti-rich MX phase (M = Nb and Ti, X = C and/or N) precipitated in grain; the other is Cr-rich $M_{23}C_6$ carbides precipitated on grain boundary. In the period of weld solidification, the liquid phase primarily solidifies, forming the dendrite γ phase. Ti and Nb segregate in the interdendritic region, causing the content of Ti and Nb to be higher than that of the dendrite trunk. When Nb and Ti accumulate to a certain extent, a eutectic reaction would occur and form γ and MX. Because the content of Nb and Ti is low in ERNiCrFe-7A filler metal, a small amount of MX phases precipitate. Due to the lower precipitation temperature, M23C6 would subsequently precipitate from γ [21]. MX phases first precipitate, consuming carbon, causing the reduction of the amount of C diffused to grain boundary and the number of $M_{23}C_6$ precipitates. The solidification sequence can be described as follows: $L \rightarrow L + \gamma \rightarrow L + \gamma + MX \rightarrow \gamma + MX \rightarrow \gamma + MX + M_{23}C_6$ [25, 26]. The precipitation of MX and $M_{23}C_6$ needs incubation

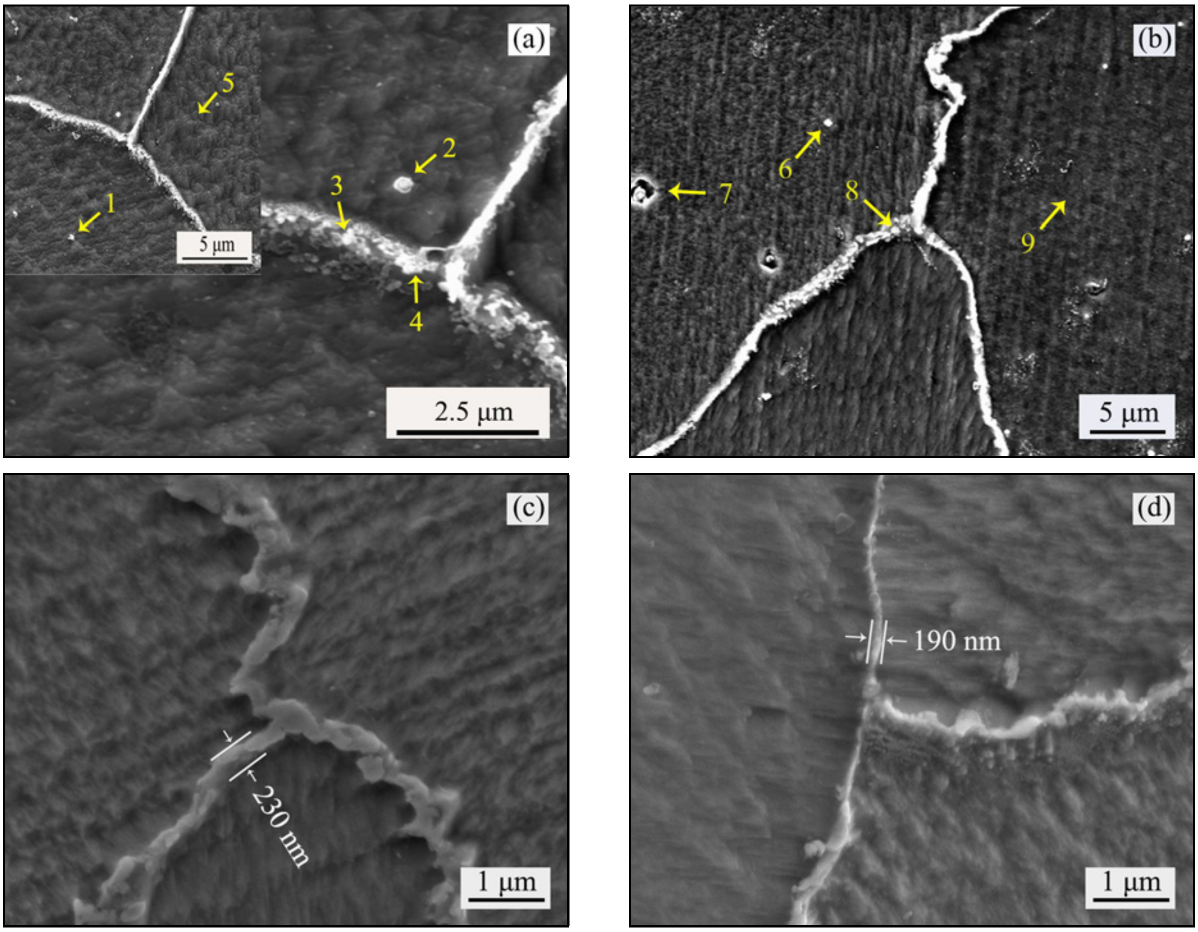

Fig. 6. SEM micrograph and EDS analysis of precipitates: (a), (c) CW-GTAW; (b), (d) HW-GTAW.

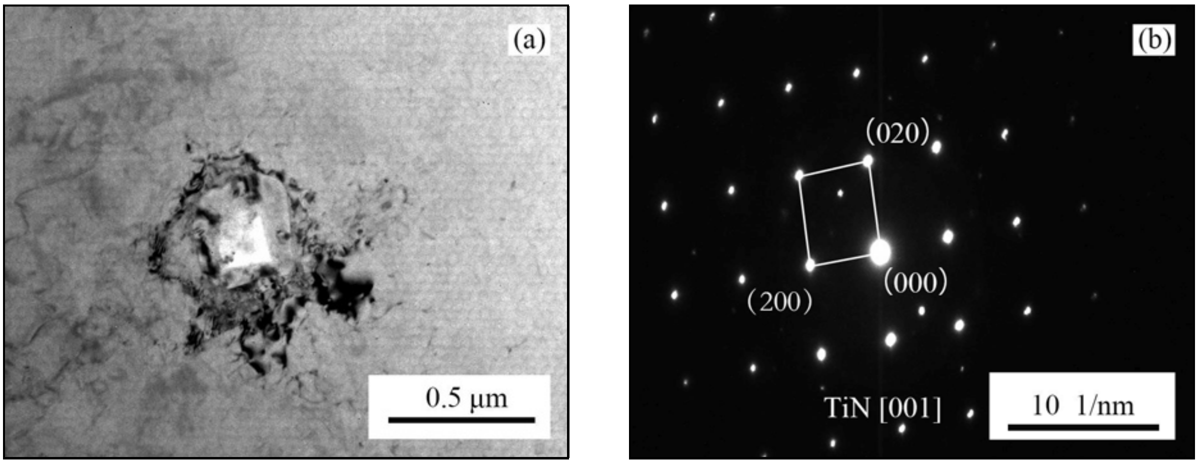

Fig. 7. TEM image of TiN: (a) Bright-field image and (b) SAED pattern.

time, while the heat input of CW-GTAW is higher than that of HW-GTAW, resulting in a slower cooling rate and more MX and $M_{23}C_6$ precipitation than HW-GTAW, especially $M_{23}C_6$.

Many nickel-base alloys undergo a severe ductility drop at temperatures between 0.5 and 0.7 of their melting temperature. When these materials are subjected to processing within this critical temperature range, a solid-state intergranular cracking phenomenon known as ductility-dip cracking (DDC) may become a serious and difficult production problem to overcome [19]. Intergranular $M_{23}C_6$ carbides are reported to influence DDC sensitivity. A large mismatch between $M_{23}C_6$ and matrix leads to stress concentra-

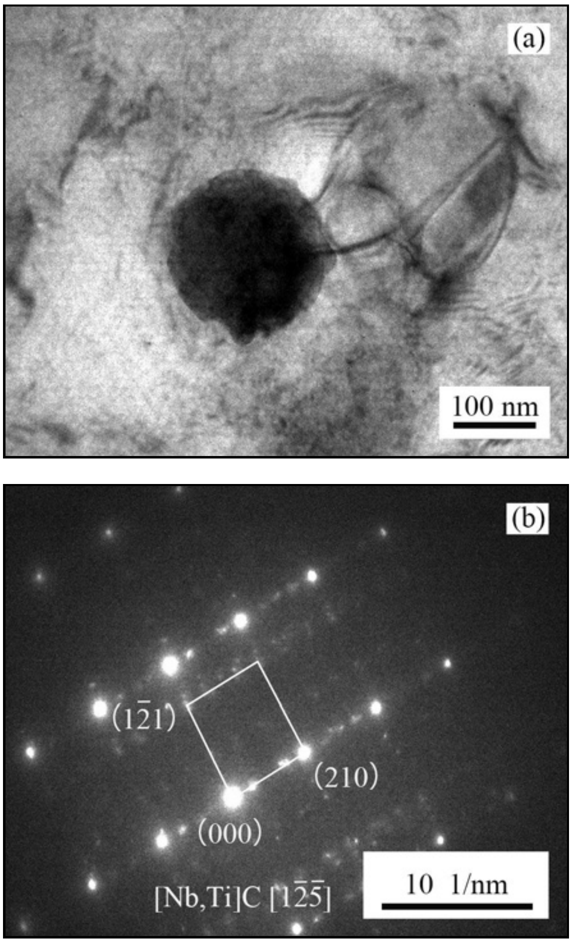

Fig. 8. TEM image of (Nb,Ti)C: (a) Bright-field image and (b) SAED pattern.

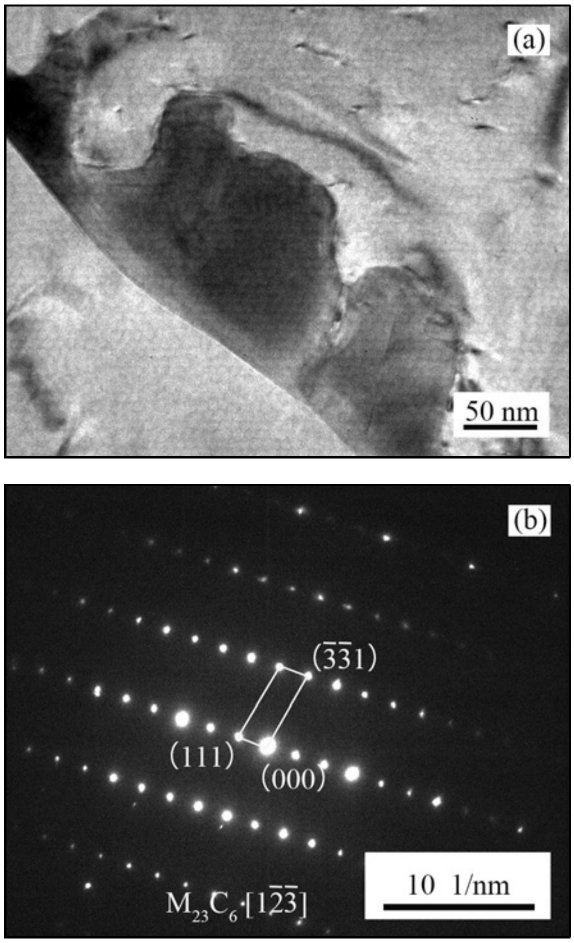

Fig. 9. TEM image of $M_{23}C_6$: (a) Bright-field image and (b) SAED pattern.

tion, which increases DDC sensitivity by cavity formation around carbides during hot deformation, especially the large and continuous $M_{23}C_6$ [14, 27–30]. So it is considered that the ERNiCrFe-7A deposited metal by CW-GTAW has higher sensitivity to DDC than that by HW-GTAW.

5. Conclusions

(1) Both CW-GTAW and HW-GTAW processes can get good quality of ERNiCrFe-7A deposited metal. The matrix of deposited metal is γ-austenite.

(2) Due to higher heat input, the columnar trend of CW-GTAW grains is more apparent than that of HW-GTAW, and the width of CW-GTAW grains is larger than that of HW-GTAW.

(3) The intragranular precipitates of deposited metal are MX phases (M = Nb and Ti, X = C and/or N), distributing in a single round shape or chain. The intergranular precipitates are Cr-rich $M_{23}C_6$ carbides distributed in flake or block. The quantities of MX and $M_{23}C_6$ by CW-GTAW are more than those by HW-GTAW.

Acknowledgements

The authors would like to acknowledge the support from the National Natural Science Foundation of China (Grant No. 52105351), Natural Science Foundation of Jiangsu Province (Grant No. BK20210890), Jiangsu Provincial Double-Innovation Doctor Program (Grant No. JSSCBS20210991), Natural Science Research Projects in Universities of Jiangsu Province (Grant No. 21KJB460015) and Youth Science and Technology Innovation Project of Jiangsu University of Science and Technology (Grant No. 1062922001).

References

[1] C. H. Yang, D. Kim, H. Lee, Carbide behavior and micro-void of Inconel 690 according to Nb content and aging temperature, Met. Mater. Int. 27 (2021) 4681–4699. https://doi.org/10.1007/s12540-021-01028-0

[2] A. Rapetti, F. Christien, F. Tancret, P. Todeschini, S. Hendili, Effect of composition on ductility dip cracking of 690 nickel alloy during multipass welding, Mater. Today Commun. 24 (2020) 101163. https://doi.org/10.1016/j.mtcomm.2020.101163

[3] B. T. Alexandrov, A. T. Hope, J. W. Sowards, J. C. Lippold, S. McCracken, Weldability studies of high-Cr, Ni-base filler metals for power generation applications, Weld World 55 (2011) 65–76. https://doi.org/10.1007/BF03321288

[4] S. L. McCracken, R. E. Smith, Behavior and Hot Cracking Susceptibility of Filler Metal 52 M (ERNiCr Fe-7A) Overlays on Cast Austenitic Stainless Steel Base Materials, Springer, 2011, pp. 333–352. https://doi.org/10.1007/978-3-642-16864-2_17

[5] Y. C. Lim, X. Yu, J. H. Cho, J. Sosa, D. F. Farson, S. S. Babu, S. McCracken, B. Flesner, Effect of magnetic stirring on grain structure refinement Part 2 – Nickel alloy weld overlays, Sci. Technol. Weld Joi. 15 (2010) 400–406. https://doi.org/10.1179/136217110X12720264008277

[6] P. R. Kannan, V. Muthupandi, K. Devakumaran, On the effect of temperature coefficient of surface tension on shape and geometry of weld beads in hot wire gas tungsten arc welding process, Mater. Today Proc. 5 (2018) 7845–7852. https://doi.org/10.1016/j.matpr.2017.11.465

[7] A. Padmanaban MR, B. Neelakandan, D. Kandasamy, A study on process characteristics and performance of hot wire gas tungsten arc welding process for high temperature materials, Mater. Res. 20 (2017) 76–87. https://doi.org/10.1590/1980-5373-mr-2016-0321

[8] S. D. Banik, S. Kumar, P. K. Singh, S. Bhattacharya, M. M. Mahapatra, Prediction of distortions and residual stresses in narrow gap weld joints prepared by hot wire GTAW and its validation with experiments, Int. J. Pres. Ves. Pip. 193 (2021) 104477. https://doi.org/10.1016/j.ijpvp.2021.104477

[9] G. Li, M. L. Zhang, J. Huang, Z. Y. Sun, Y. X. Wu, A comparative study on microstructure and properties of Inconel 52M overlays deposited by laser beam and GTA cladding, Int. J. Adv. Manuf. Technol. 81 (2015) 103–112. https://doi.org/10.1007/s00170-015-7198-8

[10] C. M. Lin, T. L. Su, K. Y. Wu, Effects of parameter optimization on microstructure and properties of GTAW clad welding on AISI 304L stainless steel using Inconel 52M, Int. J. Adv. Manuf. Technol. 79 (2015) 2057–2066. https://doi.org/10.1007/s00170-015-6875-y

[11] H. L. Ming, R. L. Zhu, Z. M. Zhang, J. Q. Wang, E. H. Han, W. K, M. X. Su, Microstructure, local mechanical properties and stress corrosion cracking susceptibility of an SA508-52M-316LN safe-end dissimilar metal weld joint by GTAW, Mater. Sci. Eng. A 669 (2016) 279–290. https://doi.org/10.1016/j.msea.2016.05.101

[12] C. M. Lin, Relationships between microstructures and properties of buffer layer with Inconel 52M clad on AISI 316L stainless steel by GTAW processing, Surf. Coat. Technol. 228 (2013) 234–241. https://doi.org/10.1016/j.surfcoat.2013.04.035

[13] S. L. Jeng, Y. H. Chang, The influence of Nb and Mo on the microstructure and mechanical properties of Ni-Cr-Fe GTAW welds, Mater. Sci. Eng. A 555 (2012) 1–12. https://doi.org/10.1016/j.msea.2012.06.017

[14] X. Wei, M. J. Xu, Q. Z. Wang, M. L. Zhang, W. H. Liu, J. J. Xu, J. M. Chen, H. Lu, C. Yu, Effect of local texture and precipitation on the ductility dip cracking of ERNiCrFe-7A Ni-based overlay, Mater. Design 110 (2016) 90–98. https://doi.org/10.1016/j.matdes.2016.07.130

[15] X. H. Zhang, P. Z. Ma, K. Zhang, J. Q. Chen, H. Chen, Study on controlling of welding seam microstructure about nickel-based high-temperature alloy by pulse TIG welding process, J. Mech. Eng. 54 (22018) 93–101. https://doi.org/10.3901/JME.2018.02.093

[16] A. J. Ramirez, J. C. Lippold, New Insight into the Mechanism of Ductility-dip Cracking in Ni-base Weld Metals, Springer, 2005, pp.19–41. https://doi.org/10.1007/3-540-27460-X_2

[17] S. McCracken, Review of Thermo-mechanical Testing and Micro-characterization Studies of Ductility-dip Cracking in Nickel-base Alloy 52 Weld Filler Metal, Proceedings of ASME Pressure Vessels and Piping Division Conference, 2005, pp. 927–937. https://doi.org/10.1115/PVP2005-71483

[18] R. G. Zhang, M. Caruso, S. Kiser, J. Crum, New 30 % Chromium-containing Ni-Cr-Fe Welding Product Provides Outstanding Resistance to PWSCC, Ductility Dip Cracking (DDC) And Meets All Other Nuclear Welding Requirements, Proceedings of NACE-International Corrosion Conference Series 7 (2012), pp. 5755–5769.

[19] A. J. Ramirez, J. W. Sowards, J. C. Lippold, Improving the ductility-dip cracking resistance of Ni-base alloys, J. Mater. Process. Tech. 179 (2006) 212–218. https://doi.org/10.1016/j.jmatprotec.2006.03.095

[20] J. S. Unfried, E. A. Torres, A. J. Ramirez, In Situ Observations of Ductility-dip Cracking Mechanism in Ni-Cr-Fe Alloys, Springer, 2011, pp. 295–315. https://doi.org/10.1007/978-3-642-16864-2_15

[21] W. L. Mo, X. Zhang, S. P. Lu, D. Z. Li, Y. Y. Li, Effect of Nb content on microstructure, welding defects and mechanical properties of NiCrFe-7 weld metal, Acta Metall. Sin. 51 (2015) 230–238. https://doi.org/10.11900/0412.1961.2014.00288

[22] J. H. Dong, D. J. Hou, J. Y. Li, R. Huang, Investigation of NbC/TiC heterogeneous nucleation interface by first-principles and experimental methods, Metals 9 (2019) 1265. https://doi.org/10.3390/met9121265

[23] H. H. Zhang, H. H. Xiong, First-principles study of NbC heterogeneous nucleation on TiC vs. TiN in microalloy steel, Ironmak. Steelmak. 47 (2020) 77–83. https://doi.org/10.1080/03019233.2018.1483613

[24] W. L. Mo, S. P. Lu, D. Z. Li, Y. Y. Li, Effects of filler metal composition on the microstructure and mechanical properties for ERNiCrFe-7 multi-pass weldments, Mater. Sci. Eng. A 582 (2013) 326–337. https://doi.org/10.1016/j.msea.2013.06.038

[25] A. J. Ramirez, C. M. Garzón, Thermodynamic and Kinetic Approach to Ductility-dip Cracking Resistance Improvement of Ni-base Alloy ERNiCrFe-7: Effect of Ti and Nb Additions, Springer, 2008, pp. 427–453. https://doi.org/10.1007/978-3-540-78628-3_22

[26] J. N. Dupont, C. V. Robino, J. R. Micheal, M. R. Notis, A. R. Marder, Solidification of Nb-bearing superalloys: Part I. Reaction sequences, Metall. Mater. Trans. A 29 (1998) 2785–2796.

https://doi.org/10.1007/s11661-998-0319-3

[27] A. J. Ramirez, J. C. Lippold, High temperature behavior of Ni-base weld metal Part II. Insight into the mechanism for ductility dip cracking, Mater. Sci. Eng. A 380 (2004) 245–258.
https://doi.org/10.1016/j.msea.2004.03.075

[28] G. A. Young, T. E. Capobianco, M. A. Penik, B. W. Morris, J. J. McGee, The mechanism of ductility dip cracking in nickel-chromium alloys, Weld J. 87 (2008) 31–43.

[29] W. L. Mo, S. P. Lu, D. Z. Li, Y. Y. Li, Effects of $M_{23}C_6$ on the high-temperature performance of Ni-based welding material NiCrFe-7, Metall. Mater. Trans. A 45 (2014) 5114–5126.
https://doi.org/10.1007/s11661-014-2439-2

[30] C. Fink, An investigation on ductility-dip cracking in the base metal heat-affected zone of wrought nickel base alloys – Part I: Metallurgical effects and cracking mechanism, Weld World 60 (2016) 939–950.
https://doi.org/10.1007/s40194-016-0370-4